

# Identification of Natural Inhibitors of SARS-CoV-2 Main Protease (M<sup>pro</sup>) via Structure-Based Virtual Screening and Molecular Dynamics Simulations

Yassir Boulaamane <sup>1</sup>, Iman Touati <sup>1</sup>, Badr-edine Sadoq <sup>1</sup>, Shilpi Agarwal <sup>2</sup>,  
Anshuman Chandra <sup>3,\*</sup>, Mohammed Reda Britel <sup>1</sup>, Amal Maurady <sup>1,4,\*</sup>

<sup>1</sup> Laboratory of Innovative Technologies, National School of Applied Sciences of Tangier, Abdelmalek Essaadi University, Tetouan, Morocco; boulaamane.yassir@etu.uae.ac.ma (Y.B.); iman.touati@etu.uae.ac.ma (I.T.); sadoq.badredine@etu.uae.ac.ma (B.-E.S.); mbritel@uae.ac.ma (M.R.B.);

<sup>2</sup> School of Physical Science, Jawaharlal Nehru University, New Delhi, 110067, India; shilpiagarwal@mail.jnu.ac.in;

<sup>3</sup> ICMR-National Institute of Malaria Research Sector 8 Dwarka, Dwarka, New Delhi, Delhi 110077; anshuman@nimr.org.in;

<sup>4</sup> Faculty of Sciences and Techniques of Tangier, Abdelmalek Essaadi University, Tetouan, Morocco; amaurady@uae.ac.ma;

\* Correspondence: boulaamane.yassir@etu.uae.ac.ma;

Scopus Author ID 36011971000

Received: 24.08.2023; Accepted: 12.05.2024; Published: 27.08.2024

**Abstract:** The ongoing COVID-19 pandemic has highlighted the urgent need for effective antiviral treatments to combat the spread of the virus. Natural products have emerged as a valuable source of potential drug candidates, given their diverse chemical structures and ability to inhibit viral replication. In this study, we selected a dataset of 356 antiviral natural products from the Ambinter chemical library and screened them for their ability to inhibit the main protease (M<sup>pro</sup>), a key target for drug development against SARS-CoV-2 using molecular docking in order to estimate their potential pharmacological activity. Furthermore, we evaluated the selected compounds' physicochemical properties and pharmacokinetic parameters to assess their drug-likeness. Finally, molecular dynamics simulations were conducted on the highest-ranking compounds to assess their stability and molecular interactions over time. Our findings indicate that the compounds Amb18482894 and Amb1953578 belonging to the flavones and the flavonolignans chemical classes exhibit strong affinity towards M<sup>pro</sup> with binding scores of  $-8.4$  and  $-8.0$  kcal/mol, respectively, which were found to be higher than the reference compound, masitinib. Moreover, better stability was observed in the studied natural compounds in complex with M<sup>pro</sup>, suggesting their potential as future drug candidates for COVID-19. This study contributes to the ongoing efforts to identify safe and effective treatments for this global health crisis.

**Keywords:** main protease (M<sup>pro</sup>); SARS-CoV-2; virtual screening; natural compounds; ADMET prediction; molecular dynamics simulations.

© 2024 by the authors. This article is an open-access article distributed under the terms and conditions of the Creative Commons Attribution (CC BY) license (<https://creativecommons.org/licenses/by/4.0/>).

## 1. Introduction

The coronavirus disease 2019 (COVID-19), caused by the severe acute respiratory syndrome coronavirus 2 (SARS-CoV-2), has caused a current pandemic with over 590 million cases and over 6.0 million deaths (<https://covid19.who.int/>) [1]. Currently, vaccines are being applied in many countries; however, it takes more time to reach levels that could control this global epidemic, which is likely to become a seasonal disease [2]. Although some antiviral drugs have received emergency authorization by various drug regulatory agencies worldwide,

their use is limited [3]. Seeing how options for treating and preventing the development of COVID-19 are limited has prompted the repurposing of available drugs as new courses of treatment [4]. Lopinavir, chloroquine, and hydroxychloroquine are among the drugs that showed in-vitro efficacy on COVID-19 [5-7]. Although several studies and clinical trials have investigated this newly found activity [8-11], these drugs still seem to fall short. The lack of effectiveness opens up new opportunities for discovering and developing new and potent therapeutics for the treatment of COVID-19.

The coronavirus enters cells by utilizing its trimeric glycosylated spike (S) protein, which consists of S1 and S2 subunits. The S1 subunit binds to the angiotensin-converting enzyme-2 (ACE2) receptor, while the S2 subunit mediates viral cell membrane fusion by forming a six-helical bundle via the two heptad repeat regions. Host cell proteases, including Transmembrane Serine Protease 2 (TMPRSS2) and endosomal cathepsins, trigger proteolytic cleavage of the S protein bound to ACE2, facilitating viral envelope-cell membrane fusion. This process releases the viral nucleocapsid into the host cell. The host cell's translation machinery recognizes the genomic RNA, synthesizing polyproteins 1a (pp1a) and 1ab (pp1ab) through ribosomal frameshifting. Main protease ( $M^{pro}$ ) cleaves these polyproteins, yielding various nonstructural proteins (nsp). Notably, nsp5 ( $M^{pro}$ ) of porcine coronavirus can modify host immune system components by cleaving NF $\kappa$ B and STAT-2, impacting IFN- $\beta$  production and expression of interferon-stimulated genes [12-14].

To date, different drug targets against SARS-CoV-2 have been identified for the development of a potential treatment, such as the RNA-dependent RNA polymerase (RdRp), papain-like protease ( $PL^{pro}$ ), and main protease ( $M^{pro}$ ) [15]. The latter ( $M^{pro}$ ) has gained relevance because, in addition to being vital for the viral life cycle, it has been observed that this enzyme prefers specific substrates not present in humans, speeding up the identification and design of new high selectivity and low toxicity covalent and non-covalent inhibitors [16].

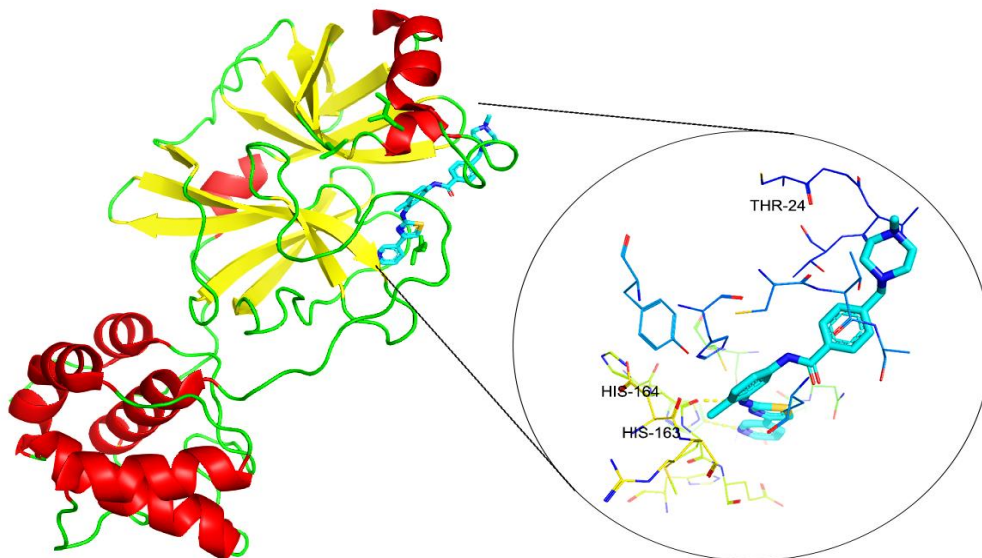


**Figure 1.** Three-dimensional structure of SARS-CoV-2  $M^{pro}$  bound with non-covalent Masitinib ligand (PDB ID: 7JU7).

$M^{pro}$ , a dimeric protein responsible for cleaving the polyprotein into various functional proteins, plays a crucial role in viral replication and transcription [17]. Consequently,  $M^{pro}$  serves as a significant drug target in the treatment of COVID-19 [18]. Structurally,  $M^{pro}$  consists of three domains: I, II, and III, with domains I and II exhibiting a chymotrypsin-like fold [19]. The substrate-binding cleft of  $M^{pro}$  is situated between domains I and II, as depicted in Figure

1.  $M^{pro}$  lacks proteolytic activity due to the unorganized substrate-binding site in its monomeric form. However, the substrate-binding site adopts a proper conformation in the dimeric form, enabling its enzymatic function [20].

In this tireless effort to develop a molecule that could be an excellent solution to the problem caused by COVID-19, this work aimed to screen a library of natural compounds from Ambinter SARL by Greenpharma (<https://www.ambinter.com/>) using virtual screening and molecular docking to guide the rational discovery and optimization of new selective inhibitors for the SARS-CoV-2 main protease ( $M^{pro}$ ).

## 2. Materials and Methods

### 2.1. Target protein selection.

There are two crystallographic structures of  $M^{pro}$  in complex with Masitinib (G65) on the RCSB PDB, 7JU7 and 7TVX, with resolutions of 1.60 Å and 2.09 Å, respectively [21,22]. To compare the superposition of the active site residues and calculate the RMSD to validate the similarity between the two structures (Figure 2A). The RMSD calculation result shows that the active site residues are well conserved between the two structures of  $M^{pro}$  with an atomic deviation value of (0.095). In this study, we chose the (PDB ID: 7JU7) structure because its resolution and Ramachandran plot show a better distribution of favorable regions with a percentage of (91.3%) (Figure 2B).

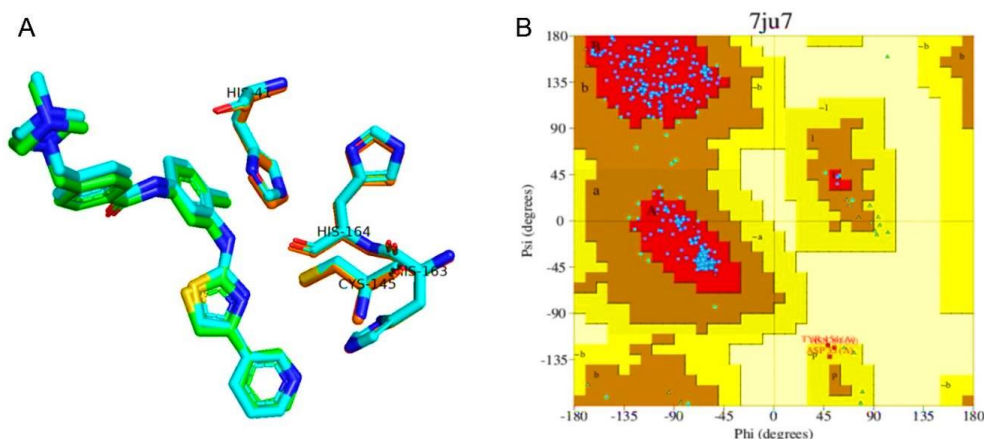


**Figure 2.** (A) Superposition of  $M^{pro}$  active site residues; (B) Ramachandran plot of  $M^{pro}$  PDB structure.

Masitinib (MST), a well-known tyrosine kinase inhibitor, had excellent inhibitory activity against  $M^{pro}$  ( $IC_{50} = 2.5\mu M$ ). The ( $MST-M^{pro}$ ) complex was resolved by X-ray crystallography and deposited in the Protein Data Bank (PDB ID: 7JU7) [23]. The crystalline structure of the ( $MST-M^{pro}$ ) complex shows that MST non-covalently binds to the two active sites on the  $M^{pro}$  homodimer. There are three key interaction sites between the active site residues of MST and  $M^{pro}$  that block the recognition of virus-coded polyproteins: (1) the pyridine-HIS hydrogen bond:163, (2) the thiazole-CYS hydrogen bond:145, and (3) the toluene-HIS  $\pi$ - $\pi$  stacking bond:41 [24]. The last two listed interactions were identified as the most relevant as they involve the two catalytic residues of the enzyme. However, upon closer examination of the complex, it can be concluded that the hydrogen bond between the thiazole ring and the side chain of Cys-145 could not occur due to the low interaction angle formed ( $94.7^\circ$ ). Although this intermolecular interaction seems unlikely, we detected during structure verification that a hydrogen bond could form between the amino group of the aminothiazole

ring and the carbonyl of the HIS main chain:164. This intermolecular hydrogen bond has a suitable distance of 3.0 Å and an angle of 158.9° to be considered a potential pharmacophore point (Figure 3).

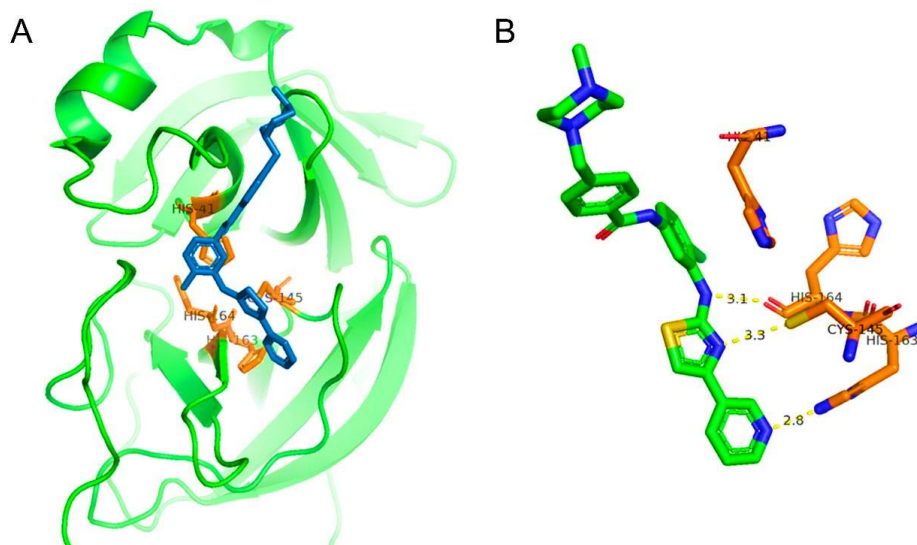


**Figure 3.** The (MST-M<sup>Pro</sup>) complex with the residues of the active site of the main protease (M<sup>Pro</sup>) of SARS-CoV-2.

### 2.2. Natural products library preparation.

In this study, we have chosen to test 350 natural molecules from the Ambinter SARL chemical library for natural products (<https://www.ambinter.com/#libraries>), which are known for their antiviral effects [25]. The ligands were downloaded from the chemical library in SDF format.

### 2.3. Virtual screening.

The result of the preparation and minimization of the 350 molecules was obtained using the PyRx software based on AutoDock Vina [26-28]. The grid box size was set to 20 x 20 x 24 with a grid center of 11.292, 5.75, and 20.679 in X, Y, and Z dimensions, respectively, and a spacing of 1 Å. Compounds displaying a binding affinity of -8.0 kcal/mol or less were taken into account for further analysis.

### 2.4. ADMET prediction.

Seven parameters were considered to evaluate the selected candidates' pharmacological properties after screening alongside Lipinski's rule of five. Human intestinal absorption (HIA), blood-brain barrier (BBB) permeability, human ether-a-go-go-related gene (hERG) inhibition, and cytochrome CYP2D6 inhibition were predicted using the SwissADME web server (<http://www.swissadme.ch/>), while toxicity parameters (AMES toxicity and carcinogenicity) were computed using the pkCSM web server (<https://biosig.lab.uq.edu.au/pkcsml/>) [29,30].

### 2.5. Molecular docking.

A molecular docking study was performed with the AutoDock 4.2.6 software, which was included in AutoDockTools for the remaining compounds [31]. The grid box parameters used to configure the molecular docking were set to 55 x 55 x 64, with a grid center of 11.527, 5.98, and 20.578 for X, Y, and Z dimensions, respectively, and a spacing of 0.375 Å.

## 2.6. Molecular dynamics simulation.

The highest-ranking compounds were selected from the molecular docking study to assess their stability under dynamic conditions and compare their behavior to the reference inhibitor. Missing side chains and loops were fixed using the CHARMM-GUI web server [32,33]. The Desmond module was used for MD simulations to investigate changes in protein structure within the solvent system [34,35]. The solvated system was created using the System Builder panel in Desmond, centered in an orthorhombic cubic box with periodic boundary conditions and filled with Single Point Charge (SPC) water molecules buffered at a distance of at least 10 Å between a protein atom and box edges [36]. The system was neutralized and maintained at an isosmotic state by adding counter-ions ( $\text{Na}^+$  and  $\text{Cl}^-$ ) and 0.15 M NaCl. The solvated system was minimized and relaxed using OPLS3e force field parameters, and a constant temperature of 300 K and pressure of 1 atm were maintained during the simulation using the Nose-Hoover thermostat algorithm and Martyna-Tobias-Klein Barostat algorithm, respectively [37,38]. The simulation was run for 100 ns, during which 1000 frames were saved. The MD simulation trajectory was analyzed using the Simulation Interaction Diagram (SID) tool [39-41].

## 3. Results and Discussion

### 3.1. Virtual screening.

Results indicate that 67 molecules showed an affinity for the main protease ( $\text{M}^{\text{Pro}}$ ) with a score less than or equal to -8.0 kcal/mol. The top twenty molecules were found to belong to the class of flavonoids, coumarins, and their derivatives. The analytical evaluation of the results of the pharmacokinetics and the re-docking of these 67 molecules will allow us to monitor and predict the ability of these classes of biomolecules to be inhibitors of the SARS-CoV-2 ( $\text{M}^{\text{Pro}}$ ) protease.

### 3.2. ADMET prediction results.

To be effective as a medication, a potent molecule must reach its target in the body at a sufficient concentration and remain in a bioactive form long enough for the expected biological events to occur [42]. In addition to Lipinski's rule of five, six pharmacokinetic parameters were considered to evaluate the pharmacological activity of the selected candidates, as shown in Table 1. Human intestinal absorption (HIA) is a parameter designed to predict the proportion of compounds the human small intestine has absorbed. A molecule with less than 30% absorbance is considered poorly absorbed. Blood-brain barrier permeability (BBB) describes the ability of a given molecule to reach the brain; a BBB value greater than 0.3 is indicative that the molecule can easily cross the blood-brain barrier, while molecules with values less than -1 are considered poorly distributed to the brain. Cytochrome CYP2D6 Inhibition (CYP2D6 inhibitor) is responsible for the metabolism of many drugs. However, P450 inhibitors can significantly alter the pharmacokinetics of these drugs. It is, therefore, important to evaluate whether a given compound is likely to be a cytochrome P450 inhibitor. The main isoform responsible for drug metabolism is CYP2D6. Human Ether-à-go-go-related gene (hERG) inhibition is the main cause of acquired long QT syndrome, leading to deadly ventricular arrhythmia. AMES toxicity test is a widely used method for evaluating the mutagenic potential of a compound using bacteria. A positive test indicates that the compound

is mutagenic and may act as a carcinogen, while carcinogenicity refers to a highly toxic endpoint of chemical compounds in drug development. Results indicate that a total of 8 molecules (Table 1) had a good pharmacokinetic profile, making them promising drug candidates.

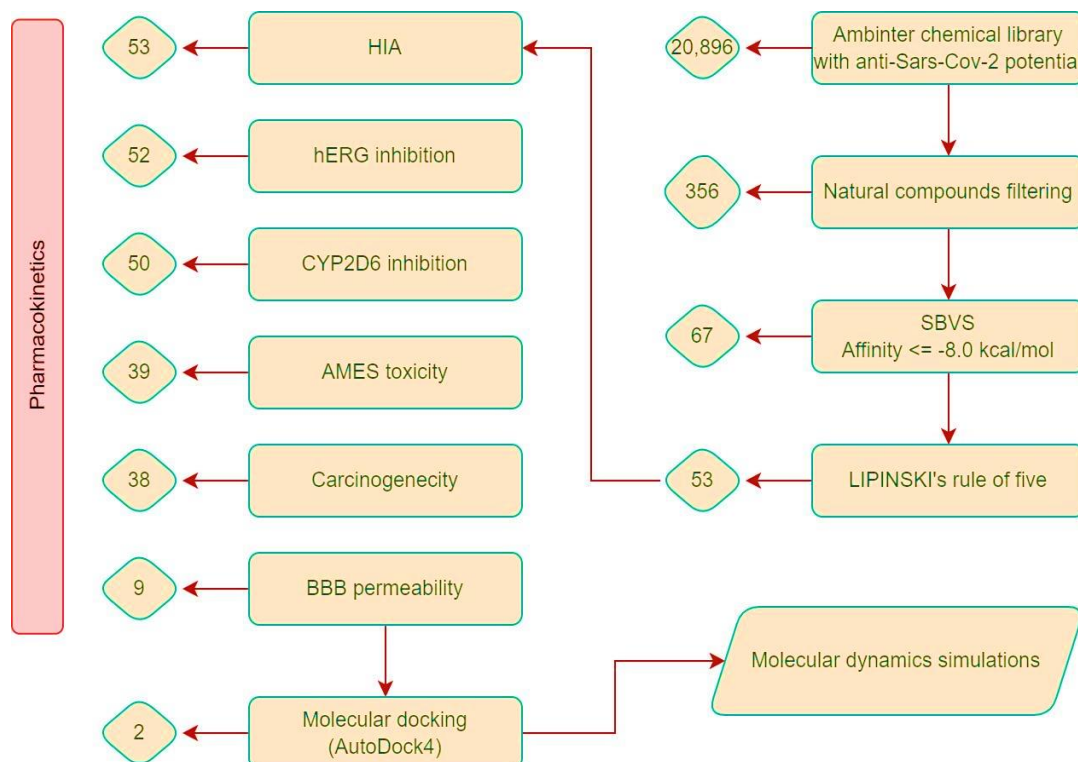
**Table 1.** ADME/Toxicity prediction results of the selected biomolecules.

Ambinter ID	ADME				Toxicity	
	HIA	BBB	CYP2D6 inhibitor	hERG inhibitor	AMES toxicity	Carcinogenicity
Rule	>30 %	< -1	(NO)	(NO)	(NO)	[0,0.7]
Masiitinib	91.71	-1.344	No	No	No	0.051
Amb18482225	93.907	-1.122	No	No	No	0.147
Amb18482894	69.246	-1.174	No	No	No	0.317
Amb18481507	62.236	-1.015	No	No	No	0.175
Amb1953578	66.913	-1.332	No	No	No	0.334
Amb17991925	58.96	-1.314	No	No	No	0.307
Amb18481638	43.765	-1.295	No	No	No	0.481
Amb22366827	51.289	-1.359	No	No	No	0.484
Amb29566134	93.515	-1.115	No	No	No	0.047

HIA: Human intestinal absorption; BBB: Blood-brain barrier permeability; CYP2D6 inhibitor: Cytochrome P450 inhibition; hERG inhibitor: Human Ether-à-go-go-Related Gene inhibitor; Ames toxicity: Mutagenicity test; Carcinogenicity: prediction of highly toxic endpoint of chemical compounds.

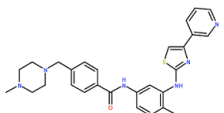
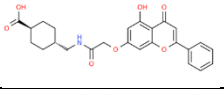
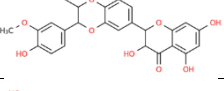
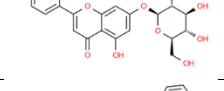
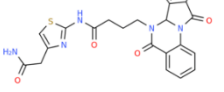
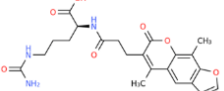
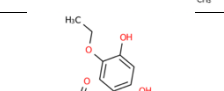
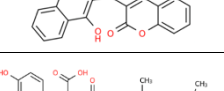
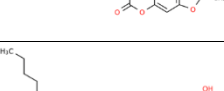
### 3.3. Molecular docking results.

The remaining compounds from the virtual screening and ADMET prediction study were selected and validated through molecular docking, as shown in Figure 4. The best-selected compounds have an affinity ranging from -7.2 to -8.4 Kcal/mol and establish hydrogen bonds with Cys-145 and His-41, the two catalytic residues of the enzyme (Table 2). It is also important to mention that these molecules form hydrophobic bonds, particularly of the Van der Waals, Pi-Pi-stacked, Pi-sigma, and Pi-alkyl types with different amino acids such as His-41, Cys-145, Met-:49, Phe-140, His-163, and Glu-166, as displayed in Figure 5.



**Figure 4.** Workflow is used for the multi-stage virtual screening of natural M<sup>pro</sup> inhibitors.

**Table 2.** Molecular docking-based virtual screening results and the resulting protein-ligand interactions.

Compound	Chemical structure	Binding score (kcal/mol)	H bonds	Aromatic interactions
Masitinib		-7.7	Gln-189	Met-49 Met-165
Amb18482894		-8.4	Tyr-54 Cys-145 Asp-187	His-41 Met-49
Amb1953578		-8.0	Leu-141 Glu-166 Arg-188	His-41 Met-165
Amb22366827		-8.0	Gln-166 Arg-188	His-41 Cys-145 Met-165
Amb29566134		-8.0	Ser-144 Glu-166	Cys-44 Met-49
Amb18481638		-7.8	Gln-189 Thr-190	His-41 Met-49
Amb18482225		-7.6	His-164 Val-186 Arg-188	Cys-44 Met-49
Amb18481507		-7.6	Gln-189 Thr-190	His-41 Met-49
Amb17991925		-7.2	Leu-141 Glu-66	His-41 Met-165

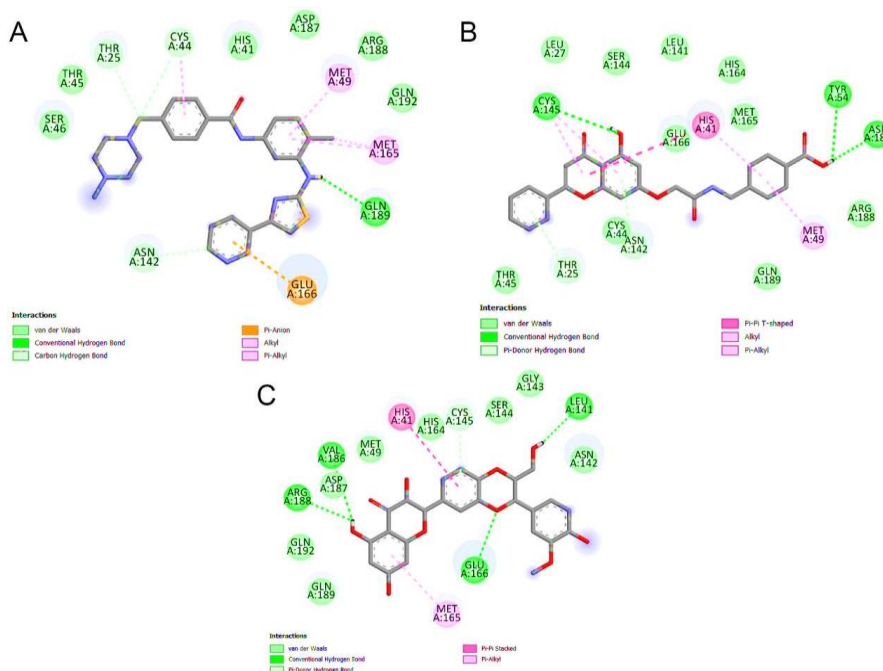


**Figure 5.** 2D plots of protein-ligand interactions of the reference drug, (A) Masitinib and the proposed candidates: (B) Amb18482894; (C) Amb1953578 using Discovery Studio Visualizer.

### 3.4. Molecular dynamics analysis.

A molecular dynamics simulation was performed to gain insights into the potential impact of selected natural compounds and a reference inhibitor, masitinib, on the structural stability of Mpro protein. This approach aimed to evaluate potential perturbations in the protein's structural integrity.

#### 3.4.1. Root-mean-square deviation.

The selected natural products' stability assessment was based on various parameters, including the measurement of conformational changes in the given complexes over time using the protein RMSD of the C-alpha backbone. This method determined whether the simulation had equilibrated and if its fluctuations towards the end of the simulation were around some thermal average structure compared to the initial structure obtained from the molecular docking study of 0 ns as a reference. Figure 6 displays the time evolution of the RMSD profiles for the C-alpha backbone of the protein and the ligand for all complexes. The RMSD analysis was performed on the C-alpha backbone of M<sup>pro</sup> in complex with the reference inhibitor masitinib. The results showed that the RMSD increased to 2.8 Å for the first 40 ns and then remained stable, with fluctuations averaging around 2.0 Å for the rest of the simulation. The same pattern was observed for Amb18482894 and Amb1953578, with the RMSD increasing during the first 40 ns before stabilizing at 2.4 Å.

Regarding the ligands, the RMSD of masitinib fluctuated around 1.5 Å and 3.5 Å during the simulation, which is considered acceptable. However, for the more flexible ligand, Amb18482894, the RMSD remained stable for the first 50 ns with minimal fluctuations of 0.6 Å but then displayed a sudden spike in RMSD up to 4.2 Å. This spike may indicate a conformational change needed for the ligand to bind to the protein. Finally, for Amb1953578, the RMSD remained stable for 80 ns before reaching 3.2 Å, suggesting that the ligand-protein complex reached a stable conformation.

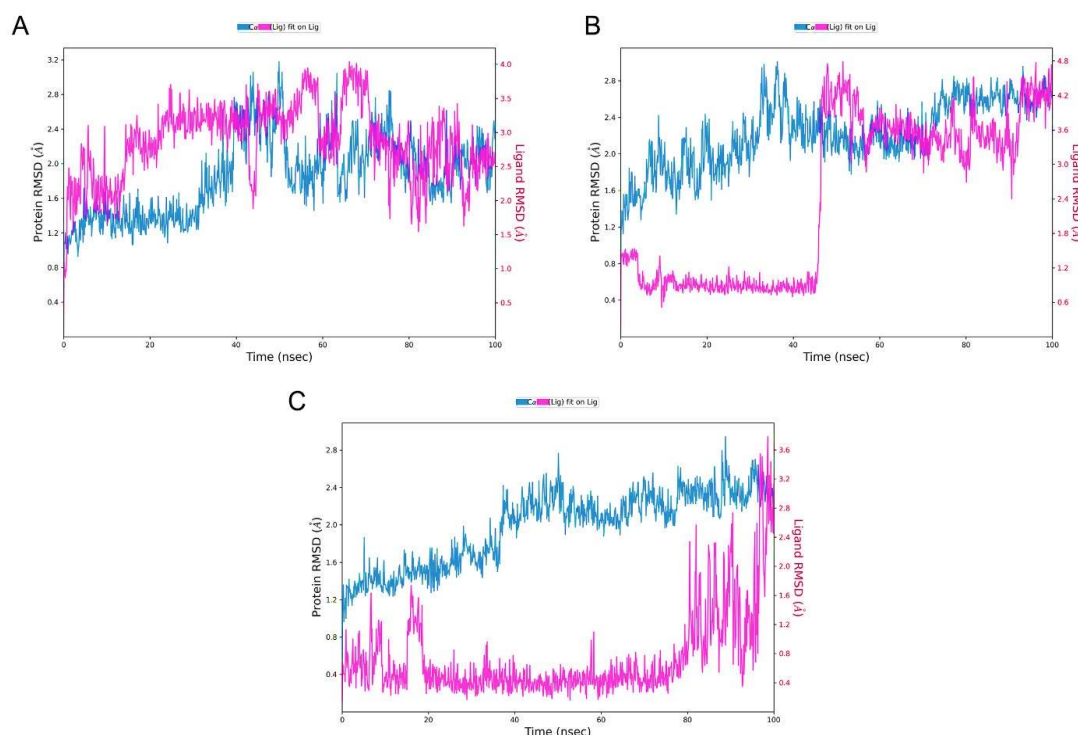


**Figure 6.** RMSD analysis of C-alpha backbone and ligands during MD simulation of the selected compounds: (A) Masitinib; (B) Amb18482894; (C) Amb1953578 with M<sup>pro</sup> target.



### 3.4.2. Root-mean square fluctuation.

The RMSF analysis provides valuable insights into local changes along the protein chain during an MD simulation. It is calculated by measuring the motion of each residue around its initial position throughout the trajectory, and it provides information about the flexibility of different regions of the protein. Figure 7 shows the RMSF plots of the C-alpha backbone for the selected complexes, highlighting the flexibility and mobility of each amino acid throughout the simulation; the green vertical lines represent the amino acids that make contact with the ligands. The observation of similar RMSF patterns in all three complexes is expected since they all involve the same protein with different ligands. The high RMSF values at the ends of the protein can be explained by the fact that these regions are generally less structured and have more freedom of movement, allowing for higher fluctuations. The region between 160 and 180, where the maximum RMSF value was observed, is of particular interest as it contains amino acids involved in ligand binding. The high RMSF values in this region suggest it is more flexible and dynamic than the surrounding areas, which could be advantageous for accommodating different ligands. However, it is also possible that the flexibility of these amino acids could lead to instability of the protein-ligand complex, which would be unfavorable.

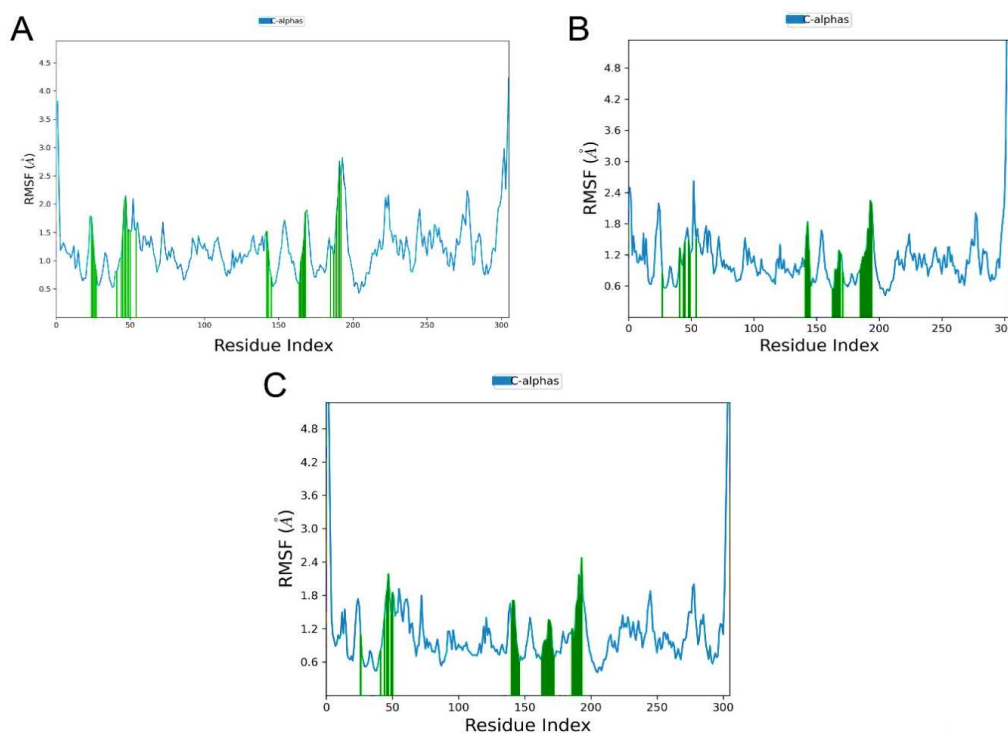


**Figure 7.** RMSF plots during MD simulation of the selected compounds: (A) Masitinib; (B) Amb18482894; (C) Amb1953578 with M<sup>pro</sup> target. Vertical green-colored lines represent protein residues that interact with the ligands.

### 3.4.3. Protein-ligand interactions.

Protein-ligand contacts were analyzed throughout the simulation to better understand each residue's role in the binding site of the protein-ligand complexes. The resulting protein-ligand interaction diagrams are presented in Figure 8. Upon analyzing the reference complex, it was observed that masitinib formed several hydrogen bonds, particularly with Glu-166, Gln-189, and Thr-190. Hydrophobic interactions were also noted, mainly involving His-41, Met-49, and Met-165. Similar interaction profiles were observed for Amb18482894, with Glu-166 consistently bound through a hydrogen bond, albeit slightly weaker than in the masitinib-M<sup>pro</sup>

complex. In the case of Amb1953578, Glu-166 was observed to be present throughout the simulation time, indicating the stability of this compound. These findings suggest that Glu-166 is a key residue involved in binding all three ligands to the M<sup>Pro</sup> protein. However, subtle differences in the strength of the hydrogen bonding interactions between Glu-166 and the ligands may account for the variations in binding affinity observed between the different complexes. Additionally, the hydrophobic interactions with His-41, Met-49, and Met-165 observed in the Masitinib-M<sup>Pro</sup> complex may also play a role in stabilizing the protein-ligand complex.

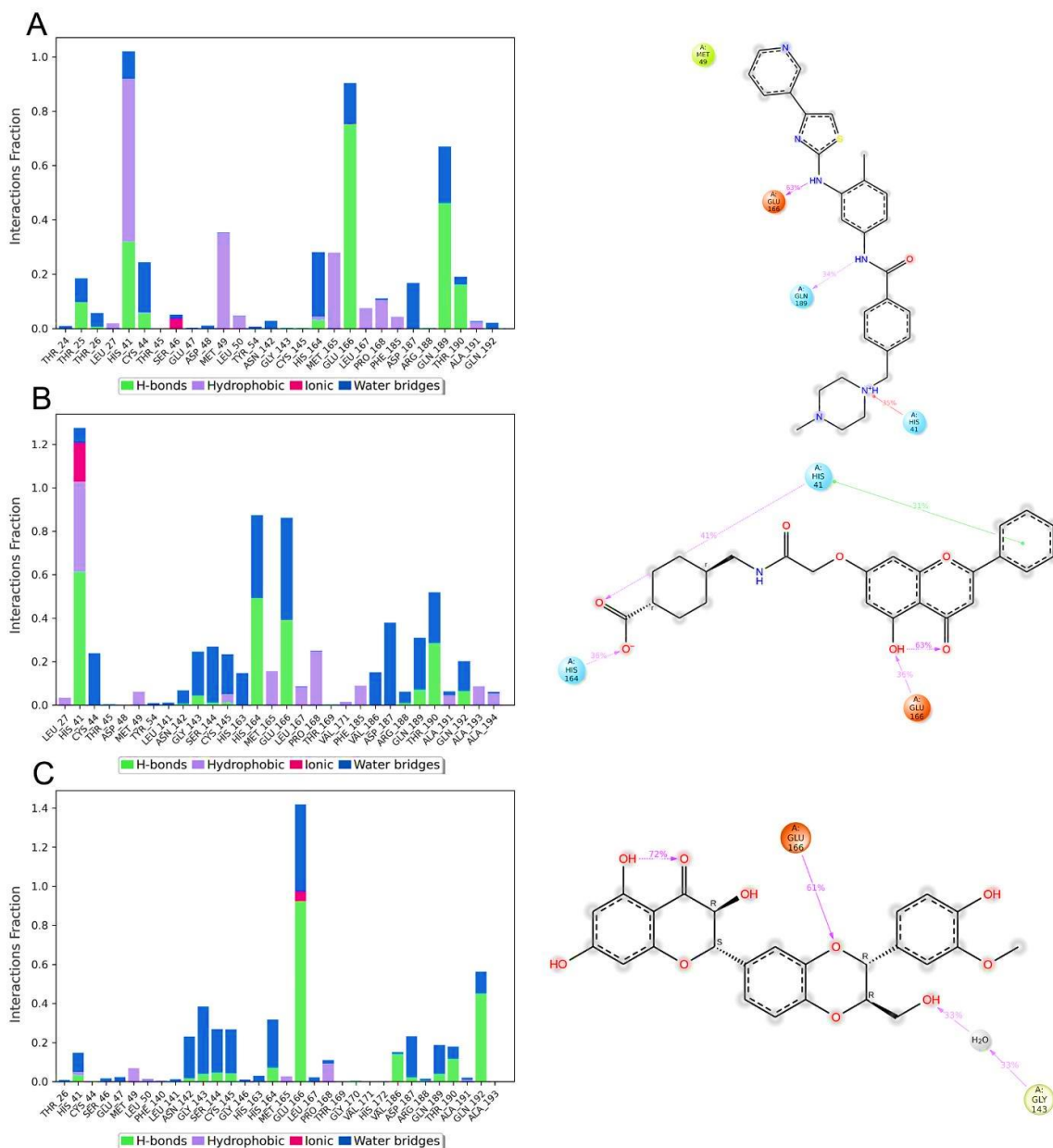


**Figure 8.** Protein-ligand interactions diagrams and 2D representation of the selected compounds: (A) Masitinib; (B) Amb18482894; (C) Amb1953578 throughout the MD simulation.

### 3.4.4. Dynamic cross-correlation matrices.

A heatmap is generated by plotting dynamic cross-correlation matrices (DCCMs), illustrating atomic motions with robust correlations through elevated correlation values [43]. Positive correlations in the DCCM between specific atom pairs indicate synchronized motions, implying simultaneous movement over time. Conversely, negative correlations signify anti-

correlated motions, suggesting that alterations in one atom's position correspond to opposing changes in another atom's position at a subsequent time [44]. In Figure 9, the DCCM plots display cross-correlations among residues of the M<sup>Pro</sup> protein (complexes A, B, and C). All three complexes exhibit strong correlations along the diagonal, indicating coordinated movements within each complex. Also, distinctive off-diagonal correlations suggest specific interactions or coordinated motions between regions. In Complex A (Masitinib), strong positive correlations appear in two main blocks (residues 50-150 and 200-300), implying the formation of distinct, cooperatively moving structural units. Complex B (Amb18482894) displays a more dispersed correlation pattern, with smaller blocks of positively correlated residues, suggesting a potentially more flexible or dynamic structure compared to Complex A. In Complex C (Amb1953578), a prominent cross-shaped pattern of positive correlations centered around residue 200 indicates a central hub of coordinated motion involving residues from different parts of the complex. Notably, Residue 150 consistently exhibits weak or negative correlations in all three complexes, suggesting it may represent a relatively static or independent region within the protein structure. A comparison of Complexes A and B reveals some similarities in correlation patterns, implying shared structural features or modes of motion, while Complex C exhibits a distinct pattern, indicating unique conformational dynamics.

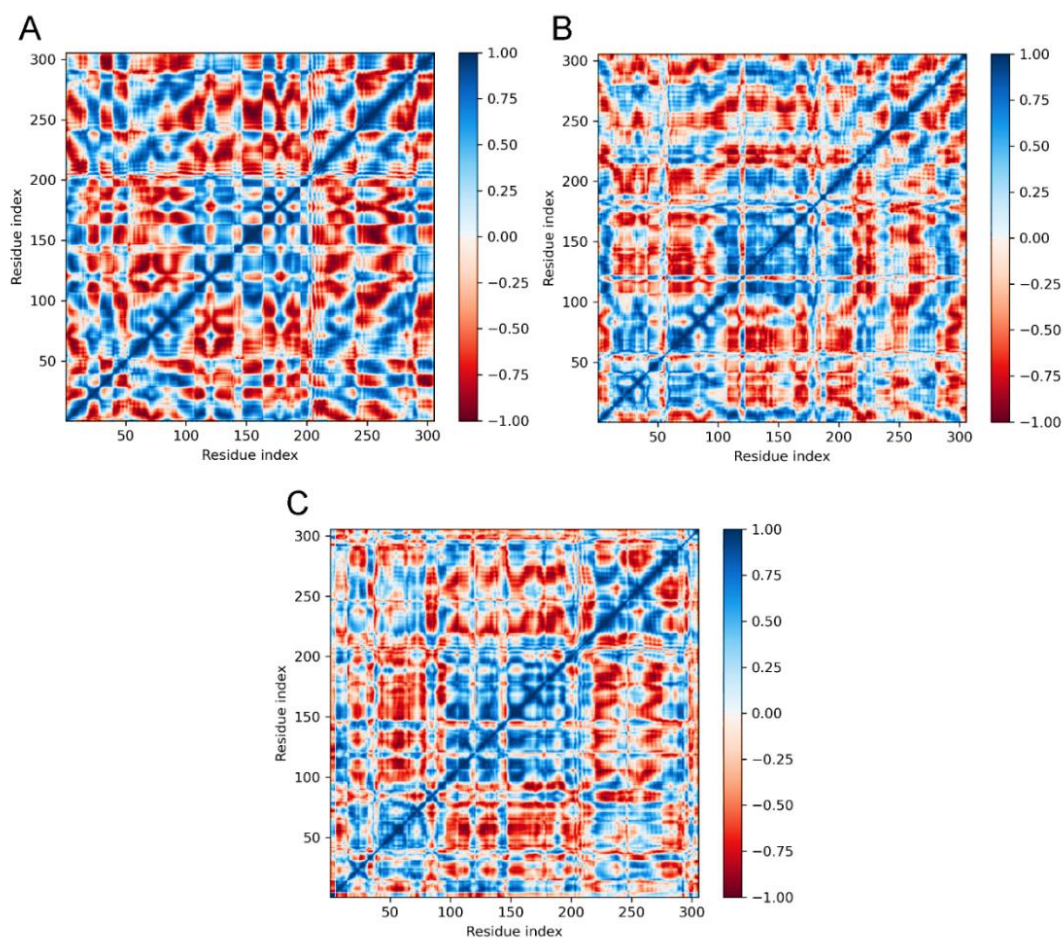


**Figure 9.** DCCM plots of the selected compounds: (A) Masitinib; (B) Amb18482894; (C) Amb1953578 throughout the MD simulation.

This work aimed to screen the natural product library (Ambinter SARL by Greenpharma) using virtual screening and molecular docking to guide the rational design of new selective inhibitors for the main protease of SARS-CoV-2 (M<sup>Pro</sup>). Upon analysis of the

molecular docking results, most molecules interact with the amino acids involved in catalytic activity, namely His-41, Cys-145, His-163, and His-164. The hydrophobic interaction of the Cys-145 residue proved to be the most favorable. Additionally, most of the selected compounds have a significant affinity for binding with the main protease (M<sup>Pro</sup>) of SARS-CoV-2 compared to our reference non-covalent inhibitor (Masitinib). The best profiles of interactions with energies are observed in molecules Amb1953578, Amb18481638, and Amb29566134. These molecules may have more potential for inhibiting SARS-CoV-2 (M<sup>Pro</sup>).

#### 4. Conclusion

Several drugs like remdesivir, molnupiravir, and paxlovid have been effective in treating certain cases. However, we need to explore natural compounds for their antiviral properties to address the current crisis and prepare for future pandemics. This study evaluated selected natural compounds' interaction and inhibition potential against the SARS-CoV-2 virus. Three compounds, Amb1953578 (Silibinin), Amb18481638, and Amb29566134, showed satisfactory binding to the target and correlated well with experimental data. We also identified key residues involved in inhibition and selectivity against SARS-CoV-2. Silibinin, extracted from milk thistle, is known for its anti-hepatotoxic properties. These promising findings suggest these compounds should be further tested as potential antiviral drugs against SARS-CoV-2.

#### Funding

This research received no external funding.

#### Acknowledgments

We would like to thank Francisco Javier Luque Garriga, Professor in the Department of Chemical Physics, University of Barcelona, Spain, for his assistance. His contribution is sincerely appreciated and gratefully acknowledged.

#### Conflicts of Interest

The authors declare no conflict of interest.

#### References

1. Shi, Y.; Wang, G.; Cai, X.P.; Deng, J.W.; Zheng, L.; Zhu, H.H.; Zheng, M.; Yang, B.; Chen, Z. An overview of COVID-19. *J. Zhejiang Univ. Sci. B* **2020**, *21*, 343-360, <https://doi.org/10.1631%2Fjzus.B2000083>.
2. Zhu, N.; Zhang, D.; Wang, W.; Li, X.; Yang, B.; Song, J.; Zhao, X.; Huang, B.; Shi, W.; Lu, R.; Niu, P.; Zhan, F.; Ma, X.; Wang, D.; Xu, W.; Wu, G.; Gao, G.F.; Tan, W. A Novel Coronavirus from Patients with Pneumonia in China, 2019. *N. Engl. J. Med.* **2020**, *382*, 727-733, <https://doi.org/10.1056/nejmoa2001017>.
3. Zhao, Y.; Yu, B.; Yu, G.; Li, W. Study on the water-heat coupled phenomena in thawing frozen soil around a buried oil pipeline. *Appl. Therm. Eng.* **2014**, *73*, 1477-1488, <https://doi.org/10.1016/j.applthermaleng.2014.06.017>.
4. Martinez, M.A. Lack of Effectiveness of Repurposed Drugs for COVID-19 Treatment. *Front. Immunol.* **2021**, *12*, 635371, <https://doi.org/10.3389/fimmu.2021.635371>.
5. Amani, B.; Khanijahani, A.; Amani, B. Hydroxychloroquine plus standard of care compared with standard of care alone in COVID-19: a meta-analysis of randomized controlled trials. *Sci. Rep.* **2021**, *11*, 11974, <https://doi.org/10.1038/s41598-021-91089-3>.

6. Yang, Y.-Z.; Liu, L.-J.; Shi, S.-F.; Wang, J.-W.; Chen, Y.-Q.; Lv, J.-C.; Zhang, H. Effects of Hydroxychloroquine on Proteinuria in Immunoglobulin A Nephropathy. *Am. J. Nephrol.* **2018**, *47*, 145-152, <https://doi.org/10.1159/000487330>.
7. Martinez, M.A. Compounds with Therapeutic Potential Against Novel Respiratory 2019 Coronavirus. *Antimicrob. Agents Chemother.* **2020**, *64*, 10-1128, <https://doi.org/10.1128/aac.00399-20>.
8. Cointe, A.; Bonacorsi, S.; Truong, J.; Hobson, C.; Doit, C.; Monjault, A.; Bidet, P.; Birgy, A. Detection of Carbapenemase-Producing *Enterobacteriaceae* in Positive Blood Culture Using an Immunochromatographic RESIST-4 O.K.N.V. Assay. *Antimicrob. Agents Chemother.* **2018**, *62*, 10-1128, <https://doi.org/10.1128%2FAAC.01828-18>.
9. Guan, W.J.; Ni, Z.Y.; Hu, Y.; Liang, W.H.; Ou, C.Q.; He, J.X.; Liu, L.; Shan, H.; Lei, C.L.; Hui, D.S.C.; Du, B.; Li, L.J.; Zeng, G.; Yuen, K.Y.; Chen, R.C.; Tang, C.L.; Wang, T.; Chen, P.Y.; Xiang, J.; Li, S.Y.; Wang, J.L.; Liang, Z.J.; Peng, Y.X.; Wei, L.; Liu, Y.; Hu, Y.H.; Peng, P.; Wang, J.M.; Liu, J.Y.; Chen, Z.; Li, G.; Zheng, Z.J.; Qiu, S.Q.; Luo, J.; Ye, C.J.; Zhu, S.Y.; Zhong, N.S. Clinical Characteristics of Coronavirus Disease 2019 in China. *N. Engl. J. Med.* **2020**, *382*, 1708-1720, <https://doi.org/10.1056/nejmoa2002032>.
10. Magagnoli, J.; Narendran, S.; Pereira, F.; Cummings, T.H.; Hardin, J.W.; Sutton, S.S.; Ambati, J. Outcomes of Hydroxychloroquine Usage in United States Veterans Hospitalized with COVID-19. *Med* **2020**, *1*, 114-127.e113, <https://doi.org/10.1016/j.medj.2020.06.001>.
11. Wrapp, D.; Wang, N.; Corbett, K.S.; Goldsmith, J.A.; Hsieh, C.L.; Abiona, O.; Graham, B.S.; McLellan, J.S. Cryo-EM structure of the 2019-nCoV spike in the prefusion conformation. *Science* **2020**, *367*, 1260-1263, <https://doi.org/10.1126/science.abb2507>.
12. Huang, Y.; Yang, C.; Xu, X.-f.; Xu, W.; Liu, S.-w. Structural and functional properties of SARS-CoV-2 spike protein: potential antiviral drug development for COVID-19. *Acta Pharmacol. Sin.* **2020**, *41*, 1141-1149, <https://doi.org/10.1038/s41401-020-0485-4>.
13. Jackson, C.B.; Farzan, M.; Chen, B.; Choe, H. Mechanisms of SARS-CoV-2 entry into cells. *Nat. Rev. Mol. Cell Biol.* **2022**, *23*, 3-20, <https://doi.org/10.1038/s41580-021-00418-x>.
14. Zhang, J.; Xiao, T.; Cai, Y.; Chen, B. Structure of SARS-CoV-2 spike protein. *Curr. Opin. Virol.* **2021**, *50*, 173-182, <https://doi.org/10.1016/j.coviro.2021.08.010>.
15. Xia, S.; Zhu, Y.; Liu, M.; Lan, Q.; Xu, W.; Wu, Y.; Ying, T.; Liu, S.; Shi, Z.; Jiang, S.; Lu, L. Fusion mechanism of 2019-nCoV and fusion inhibitors targeting HR1 domain in spike protein. *Cell. Mol. Immunol.* **2020**, *17*, 765-767, <https://doi.org/10.1038/s41423-020-0374-2>.
16. Mercurio, N.J.; Yen, C.F.; Shim, D.J.; Maher, T.R.; McCoy, C.M.; Zimetbaum, P.J.; Gold, H.S. Risk of QT Interval Prolongation Associated With Use of Hydroxychloroquine With or Without Concomitant Azithromycin Among Hospitalized Patients Testing Positive for Coronavirus Disease 2019 (COVID-19). *JAMA Cardiol.* **2020**, *5*, 1036-1041, <https://doi.org/10.1001/jamacardio.2020.1834>.
17. Paciaroni, A.; Libera, V.; Ripanti, F.; Orecchini, A.; Petrillo, C.; Francisci, D.; Schiaroli, E.; Sabbatini, S.; Gidari, A.; Bianconi, E.; Macchiarulo, A.; Hussain, R.; Silvestrini, L.; Moretti, P.; Belhaj, N.; Vercelli, M.; Roque, Y.; Mariani, P.; Comez, L.; Spinozzi, F. Stabilization of the Dimeric State of SARS-CoV-2 Main Protease by GC376 and Nirmatrelvir. *Int. J. Mol. Sci.* **2023**, *24*, 6062, <https://doi.org/10.3390/ijms24076062>.
18. Parmar, M.; Thumar, R.; Patel, B.; Athar, M.; Jha, P.C.; Patel, D. Structural Differences In 3C-like protease (Mpro) From SARS-CoV and SARS-CoV-2: Molecular Insights for Drug Repurposing Against COVID-19 Revealed by Molecular Dynamics Simulations. *bioRxiv* **2023**, *34*, 2021-2008, <https://doi.org/10.1101/2021.08.11.455903>.
19. Jin, Z.; Du, X.; Xu, Y.; Deng, Y.; Liu, M.; Zhao, Y.; Zhang, B.; Li, X.; Zhang, L.; Peng, C.; Duan, Y.; Yu, J.; Wang, L.; Yang, K.; Liu, F.; Jiang, R.; Yang, X.; You, T.; Liu, X.; Yang, X.; Bai, F.; Liu, H.; Liu, X.; Guddat, L.W.; Xu, W.; Xiao, G.; Qin, C.; Shi, Z.; Jiang, H.; Rao, Z.; Yang, H. Structure of M<sup>pro</sup> from SARS-CoV-2 and discovery of its inhibitors. *Nature* **2020**, *582*, 289-293, <https://doi.org/10.1038/s41586-020-2223-y>.
20. Anton, D.B.; Galvez Bulhões Pedreira, J.; Zvirtes, M.L.; Laufer, S.A.; Ducati, R.G.; Goettert, M.; Saraiva Macedo Timmers, L.F. Targeting SARS-CoV-2 Main Protease (MPro) with Kinase Inhibitors: A Promising Approach for Discovering Antiviral and Anti-inflammatory Molecules against SARS-CoV-2. *J. Chem. Inf. Model* **2023**, *63*, 4138-4146, <https://doi.org/10.1021/acs.jcim.3c00324>.
21. Kouranov, A.; Xie, L.; de la Cruz, J.; Chen, L.; Westbrook, J.; Bourne, P.E.; Berman, H.M. The RCSB PDB information portal for structural genomics. *Nucleic Acids Res.* **2006**, *34*, D302-D305, <https://doi.org/10.1093/nar/gkj120>.

22. Drayman, N.; DeMarco, J.K.; Jones, K.A.; Azizi, S.-A.; Froggatt, H.M.; Tan, K.; Maltseva, N.I.; Chen, S.; Nicolaescu, V.; Dvorkin, S.; Furlong, K.; Kathayat, R.S.; Firpo, M.R.; Mastrodomenico, V.; Bruce, E.A.; Schmidt, M.M.; Jedrzejczak, R.; Muñoz-Alfía, M.Á.; Schuster, B.; Nair, V.; Han, K.-y.; O'Brien, A.; Tomatsidou, A.; Meyer, B.; Vignuzzi, M.; Missiakas, D.; Botten, J.W.; Brooke, C.B.; Lee, H.; Baker, S.C.; Mounce, B.C.; Heaton, N.S.; Severson, W.E.; Palmer, K.E.; Dickinson, B.C.; Joachimiak, A.; Randall, G.; Tay, S. Masitinib is a broad coronavirus 3CL inhibitor that blocks replication of SARS-CoV-2. *Science* **2021**, *373*, 931-936, <https://doi.org/10.1126/science.abg5827>.
23. Dubreuil, P.; Letard, S.; Ciufolini, M.; Gros, L.; Humbert, M.; Castéran, N.; et al. Masitinib (AB1010), a potent and selective tyrosine kinase inhibitor targeting KIT. *PloS one*, **2009**, *4*, e7258.
24. Gurung, A.B.; Ali, M.A.; Aljowaie, R.M.; Almutairi, S.M.; Sami, H.; Lee, J. Masitinib analogues with the *N*-methylpiperazine group replaced – A new hope for the development of anti-COVID-19 drugs. *J. King Saud Univ. Sci.* **2023**, *35*, 102397, <https://doi.org/10.1016/j.jksus.2022.102397>.
25. Iii, A.-R.B.S.; Billones, J.B. Virtual screening of natural products, molecular docking and dynamics simulations on *M. tuberculosis* S-adenosyl-L-homocysteine hydrolase. *Orient. J. Chem.* **2015**, *31*, 1859-1865, <http://dx.doi.org/10.13005/ojc/310402>.
26. Dallakyan, S.; Olson, A.J. Small-Molecule Library Screening by Docking with PyRx. In *Chemical Biology: Methods and Protocols*, Hempel, J.E., Williams, C.H., Hong, C.C., Eds.; Springer New York, New York, NY, **2015**; 243-250, [https://doi.org/10.1007/978-1-4939-2269-7\\_19](https://doi.org/10.1007/978-1-4939-2269-7_19).
27. Trott, O.; Olson, A.J. AutoDock Vina: Improving the speed and accuracy of docking with a new scoring function, efficient optimization, and multithreading. *J. Comput. Chem.* **2010**, *31*, 455-461, <https://doi.org/10.1002/jcc.21334>.
28. Boulaamane, Y.; Ahmad, I.; Patel, H.; Das, N.; Britel, M.R.; Maurady, A. Structural exploration of selected C6 and C7-substituted coumarin isomers as selective MAO-B inhibitors. *J. Biomol. Struct. Dyn.* **2023**, *41*, 2326-2340, <https://doi.org/10.1080/07391102.2022.2033643>.
29. Daina, A.; Michielin, O.; Zoete, V. SwissADME: a free web tool to evaluate pharmacokinetics, drug-likeness and medicinal chemistry friendliness of small molecules. *Sci. Rep.* **2017**, *7*, 42717, <https://doi.org/10.1038/srep42717>.
30. Pires, D.E.V.; Blundell, T.L.; Ascher, D.B. pkCSM: Predicting Small-Molecule Pharmacokinetic and Toxicity Properties Using Graph-Based Signatures. *J. Med. Chem.* **2015**, *58*, 4066-4072, <https://doi.org/10.1021/acs.jmedchem.5b00104>.
31. Morris, G.M.; Huey, R.; Lindstrom, W.; Sanner, M.F.; Belew, R.K.; Goodsell, D.S.; Olson, A.J. AutoDock4 and AutoDockTools4: Automated docking with selective receptor flexibility. *J. Comput. Chem.* **2009**, *30*, 2785-2791, <https://doi.org/10.1002%2Fjcc.21256>.
32. Jo, S.; Kim, T.; Iyer, V.G.; Im, W. CHARMM-GUI: A web-based graphical user interface for CHARMM. *J. Comput. Chem.* **2008**, *29*, 1859-1865, <https://doi.org/10.1002/jcc.20945>.
33. Boulaamane, Y.; Ibrahim, M.A.A.; Britel, M.R.; Maurady, A. *In silico* studies of natural product-like caffeine derivatives as potential MAO-B inhibitors/AA2AR antagonists for the treatment of Parkinson's disease. *J. Integr. Bioinform.* **2022**, *19*, 20210027, <https://doi.org/10.1515/jib-2021-0027>.
34. D.E. Shaw Research, Schrödinger Release. Desmond Molecular Dynamics System. Maestro-Desmond Interoperability Tools; 2020–3.
35. Boulaamane, Y.; Touati, I.; Goyal, N.; Chandra, A.; Kori, L.; Ibrahim, M.A.A.; Britel, M.R.; Maurady, A. Exploring natural products as multi-target-directed drugs for Parkinson's disease: an *in-silico* approach integrating QSAR, pharmacophore modeling, and molecular dynamics simulations. *J. Biomol. Struct. Dyn.* **2023**, 1-18, <https://doi.org/10.1080/07391102.2023.2260879>.
36. Glättli, A.; Daura, X.; van Gunsteren, W.F. Derivation of an improved simple point charge model for liquid water: SPC/A and SPC/L. *J. Chem. Phys.* **2002**, *116*, 9811-9828.
37. Rühle, V. Berendsen and nose-hoover thermostats. *Am. J. Phys.* **2007**, *575*, 1-4.
38. Sanders, J.M.; Misra, M.; Mustard, T.J.L.; Giesen, D.J.; Zhang, T.; Shelley, J.; Halls, M.D. Characterizing moisture uptake and plasticization effects of water on amorphous amylose starch models using molecular dynamics methods. *Carbohydr. Polym.* **2021**, *252*, 117161, <https://doi.org/10.1016/j.carbpol.2020.117161>.
39. Boulaamane, Y.; Jangid, K.; Britel, M.R.; Maurady, A. Probing the molecular mechanisms of  $\alpha$ -synuclein inhibitors unveils promising natural candidates through machine-learning QSAR, pharmacophore modeling, and molecular dynamics simulations. *Mol. Divers.* **2023**, 1-17, <https://doi.org/10.1007/s11030-023-10691-x>.

40. Boulaamane, Y.; Molina Panadero, I.; Hmadcha, A.; Atalaya Rey, C.; Baammi, S.; El Allali, A.; et al. Antibiotic discovery with artificial intelligence for the treatment of *Acinetobacter baumannii* infections. *Msystems*, **2024**, e00325-24.
41. Boulaamane, Y.; Kandpal, P.; Chandra, A.; Britel, M.R.; Maurady, A. Chemical library design, QSAR modeling and molecular dynamics simulations of naturally occurring coumarins as dual inhibitors of MAO-B and AChE. *J. Biomol. Struct. Dyn.* **2024**, *42*, 1629-1646, <https://doi.org/10.1080/07391102.2023.2209650>.
42. Bhandari, S.; Agrwal, A.; Kasana, V.; Tandon, S.; Boulaamane, Y.; Maurady, A.  $\beta$ -amino carbonyl derivatives: Synthesis, Molecular Docking, ADMET, Molecular Dynamic and Herbicidal studies. *ChemSelect* **2022**, *7*, e202201572, <https://doi.org/10.1002/slct.202201572>.
43. Yu, H.; Dalby, P.A. Chapter Two - A beginner's guide to molecular dynamics simulations and the identification of cross-correlation networks for enzyme engineering. In *Methods in Enzymology*, Tawfik, D.S., Ed.; Academic Press, **2020**; Volume 643, 15-49, <https://doi.org/10.1016/bs.mie.2020.04.020>.
44. Kasahara, K.; Fukuda, I.; Nakamura, H. A Novel Approach of Dynamic Cross Correlation Analysis on Molecular Dynamics Simulations and Its Application to Ets1 Dimer–DNA Complex. *PLoS ONE* **2014**, *9*, e112419, <https://doi.org/10.1371/journal.pone.0112419>.